

# Strong visible and near infrared photoluminescence from ZnO nanorods/nanowires grown on single layer graphene studied using sub-band gap excitation

Ravi K. Biroju and P. K. Giri

Citation: *Journal of Applied Physics* **122**, 044302 (2017); doi: 10.1063/1.4995957

View online: <http://dx.doi.org/10.1063/1.4995957>

View Table of Contents: <http://aip.scitation.org/toc/jap/122/4>

Published by the *American Institute of Physics*

---

---

**AIP** | Journal of  
Applied Physics

Save your money for your research.  
It's now **FREE** to publish with us -  
no page, color or publication charges apply.

Publish your research in the  
*Journal of Applied Physics*  
to claim your place in applied  
physics history.

# Strong visible and near infrared photoluminescence from ZnO nanorods/nanowires grown on single layer graphene studied using sub-band gap excitation

Ravi K. Biroju<sup>1,a)</sup> and P. K. Giri<sup>1,2,b)</sup>

<sup>1</sup>Centre for Nanotechnology, Indian Institute of Technology Guwahati, Guwahati-781039, India

<sup>2</sup>Department of Physics, Indian Institute of Technology Guwahati, Guwahati-781039, India

(Received 2 May 2017; accepted 13 July 2017; published online 28 July 2017)

Fabrication and optoelectronic applications of graphene based hybrid 2D-1D semiconductor nanostructures have gained tremendous research interest in recent times. Herein, we present a systematic study on the origin and evolution of strong broad band visible and near infrared (NIR) photoluminescence (PL) from vertical ZnO nanorods (NRs) and nanowires (NWs) grown on single layer graphene using both above band gap and sub-band gap optical excitations. High resolution field emission scanning electron microscopy and X-ray diffraction studies are carried out to reveal the morphology and crystalline quality of as-grown and annealed ZnO NRs/NWs on graphene. Room temperature PL studies reveal that besides the UV and visible PL bands, a new near-infrared (NIR) PL emission band appears in the range between 815 nm and 886 nm (1.40–1.52 eV). X-ray photoelectron spectroscopy studies revealed excess oxygen content and unreacted metallic Zn in the as-grown ZnO nanostructures, owing to the low temperature growth by a physical vapor deposition method. Post-growth annealing at 700 °C in the Ar gas ambient results in the enhanced intensity of both visible and NIR PL bands. On the other hand, subsequent high vacuum annealing at 700 °C results in a drastic reduction in the visible PL band and complete suppression of the NIR PL band. PL decay dynamics of green emission in Ar annealed samples show tri-exponential decay on the nanosecond timescale including a very slow decay component (time constant ~604.5 ns). Based on these results, the NIR PL band comprising two peaks centered at ~820 nm and ~860 nm is tentatively assigned to neutral and negatively charged oxygen interstitial ( $O_i$ ) defects in ZnO, detected experimentally for the first time. The evidence for oxygen induced trap states on the ZnO NW surface is further substantiated by the slow photocurrent response of graphene-ZnO NRs/NWs. These results are important for tunable light emission, photodetection, and other cutting edge applications of graphene-ZnO based 2D-1D hybrid nanostructures. *Published by AIP Publishing.*  
[\[http://dx.doi.org/10.1063/1.4995957\]](http://dx.doi.org/10.1063/1.4995957)

## I. INTRODUCTION

Graphene is being recognized as a unique two dimensional (2D) material platform for the fabrication of vertical semiconductor nanorod (NR) and nanowire (NW) hybrid nanostructures, and it has triggered immense interest in the field of nanotechnology.<sup>1</sup> Various 1D and 2D semiconductor nanostructures have been fabricated on the graphene buffer layer, in which graphene may form the atomic Schottky barrier and enhance the photoresponse of the heterostructure for specialized optoelectronic application.<sup>2–4</sup> Since single layer graphene (SLG) has only 2.7% of absorption over the wide range of visible to near-infrared (NIR) spectra and very high charge carrier mobility, combining it with 1D or 2D semiconductor nanostructures that are grown on the graphene substrate may enhance the optoelectronic properties of the hybrid nanostructures. New optical functionalities and ultra-fast photoresponses have been achieved with semiconductor

NRs/NWs grown on the single layer (SLG) and few layer graphene (FLG) substrates for multifunctional optoelectronic device applications.<sup>3,5,6</sup> However, the existence of lattice defects is natural in the material fabrication process, and controlling the defects in 2D and 1D hybrid nanostructures is of paramount importance for successful applications. Hence, it is desirable to achieve defect engineering on these hybrid nanostructures to explore their enhanced functionalities. Recently, the defect induced fast photoresponse in graphene in the IR region was accomplished by Gowda *et al.* by introducing defect sites (wrinkles) in FLG and further improved with the FLG—multiwalled carbon nanotube hybrid structure.<sup>7</sup> In this prospect, understanding the photoluminescence (PL) properties of physical vapor deposited (PVD) semiconducting NRs/NWs on the graphene layer in the visible to near infrared (NIR) region is one of the interesting and upcoming issues to gain insight into the enhanced properties of 2D–1D integrated hybrid nanostructures for suitable optoelectronic devices.<sup>3,8–10</sup>

Among different semiconductor nanostructures, ZnO NR/NW is very versatile and one of the best candidates for photosensitive devices to operate in the UV-visible to near-infrared (NIR) region, particularly for enhanced UV

<sup>a)</sup>Present address: TIFR-Center for Interdisciplinary Sciences, Tata Institute of Fundamental Research, 21-Brundavan Colony, Narsingi, Hyderabad-500075, Telangana State, India. Electronic mail: ravikb@tifrh.res.in.

<sup>b)</sup>Author to whom correspondence should be addressed: giri@iitg.ernet.in. Telephone: +91 361 2582703.

photodetection and white light emitting diodes.<sup>11–13</sup> ZnO is a direct band gap (3.3 eV) semiconducting material with high exciton binding energy (60 meV) having extraordinary photophysical properties. In particular, ZnO NRs/NWs have huge light absorption in the UV region due to their large band gap and large surface to volume ratio and show pronounced UV and visible PL and fast photocurrent responses that are suitable for photoconductive applications.<sup>14</sup> Fabrication of the 1D ZnO NRs/NWs on an extremely conductive and highly transparent 2D graphene sheet has been exploited by the research community to study the improved optical properties of integrated hybrid nanomaterials.<sup>15–17</sup> Understanding on the physics of defect induced visible and NIR PL from ZnO NRs/NWs is intensely debated in the research community in order to implement it in various applications.<sup>18–21</sup> Wang *et al.*<sup>18</sup> reported a NIR PL centered at 756 nm from ZnO microspheres grown by a hydrothermal method, and it was attributed to the donor-acceptor transitions between oxygen vacancies ( $V_O$ ) and Zn vacancies ( $V_{Zn}$ ) and/or the radiative recombination of shallowly trapped electrons with deeply trapped holes at oxygen interstitials ( $O_i$ ). However, to our knowledge, no NIR PL has been reported on VLS grown ZnO NRs/NWs that are grown at relatively higher temperature, and thus, its detailed origin is least understood in the literature. In particular, no NIR PL has been reported for ZnO NRs/NWs grown on the graphene layer. For systematic studies on the origin of NIR PL bands from different graphene-ZnO hybrid nanostructures, we monitored the PL by annealing the samples either in vacuum or in an Ar gas atmosphere at two different temperatures. There are no reports on the PL emissions from graphene based ZnO NRs/NWs with sub-band excitation wavelengths to probe the optical properties of the resultant hybrid nanostructures. However, numerous UV-visible and a few NIR PL studies have been carried out on the ZnO nanostructures grown by conventional methods.<sup>18,22,23</sup> The physical origin and the mechanism on the broad band visible and NIR emissions in the range of 600–900 nm are still not understood clearly.

In the present work, PL studies in the visible and NIR wavelength region on ZnO NRs/NWs grown on the graphene layer have been carried out systematically using both above band gap (325 nm) and sub-band gap (405 nm) laser excitations. Besides the characteristic band edge UV emission, we have found very strong and broad band visible PL from all the samples, and the results are consistent for two different excitation wavelengths. Besides these, there is a strong NIR PL band in the range of 800–900 nm, reported for the first time. The evolution of the NIR PL bands is monitored by annealing the samples in different gas environments. Further, morphological and crystalline quality of the graphene-ZnO NR/NW hybrids was studied by high resolution FESEM and X-ray diffraction (XRD), respectively. The local chemical environment and elemental composition were analyzed using X-ray photoelectron spectroscopy (XPS) to support the conclusions of the PL analysis. Further, photoconductivity (PC) and photoresponse studies on these samples revealed high photocurrent and a slow photoresponse with UV excitation, which supports the defect dominated nature of the photophysical process due to the surface traps on the ZnO NRs/NWs. The origin of

various PL emissions in graphene-ZnO NR/NW hybrid nanostructures is elucidated.

## II. EXPERIMENT

### A. Chemical vapor deposition (CVD) growth of graphene and ZnO NRs/NWs

Large area single layer and few layer graphene was synthesized on a copper (Cu) foil of thickness 25  $\mu\text{m}$  (Alfa Aesar, 99.99% purity) using an in-house developed thermal chemical vapor deposition (CVD) setup. As-grown graphene on the Cu foil was transferred onto the Si/SiO<sub>2</sub> and quartz substrates by a wet transfer technique. The quality of the graphene layer was assessed by micro-Raman spectroscopy and high resolution transmission electron microscopy (HRTEM) analyses. The full experimental details on the graphene growth and clean transfer of graphene were reported elsewhere.<sup>15,24</sup>

Subsequently, various ZnO nanostructures were grown on the above prepared graphene substrates by using a physical vapor deposition system for different pretreated substrates. At first, an  $\sim 5$  nm thick Au film was deposited on the graphene substrate, bare oxidized Si (Si/SiO<sub>2</sub>), and quartz substrates by radio frequency (RF) magnetron sputtering. Some of the Au coated substrates were treated by rapid thermal annealing (RTA) at 600 °C in an Ar atmosphere to form Au nanoparticles/islands. Commercial activated zinc (Zn) powder (purity  $\sim 99\%$ , Aldrich) was used as a source material for the vapor phase growth of ZnO nanostructures. 100 mg of Zn powder was taken in an alumina boat and placed at the center of a horizontal quartz tube, and the assembly was placed inside a horizontal muffle furnace. The Au coated graphene substrates with and without RTA treatment were placed downstream  $\sim 5$  cm away from the source. Initially, the quartz chamber was pumped down to a pressure of  $\sim 10^{-3}$  mbar. The source temperature was kept at  $\sim 550$  °C, the substrate temperature was at 540 °C, and throughout the temperature ramp, 300 standard cubic centimeters per minute (sccm) of Ar gas was flushed until it reached the set point with a heating rate 18 °C/min in order to prevent the oxidation of the graphene substrate. When the furnace reached the source temperature (550 °C), 20 sccm of O<sub>2</sub> gas was introduced and the gas pressure inside the chamber was maintained at 1.4 mbar for the growth time of 50 min. After the completion of reaction, the furnace was cooled down to room temperature. ZnO deposition was carried out on three different sets of substrates under identical growth conditions: (i) Si/SiO<sub>2</sub>/graphene/Au NPs (sample named: GRZNR), (ii) Si/SiO<sub>2</sub>/graphene/Au film (GRZNW), and (iii) Si/SiO<sub>2</sub>/Au film (ZNW). A more detailed account of the structural evolution and the growth mechanism of the ZnO nanostructures has been reported elsewhere.<sup>15</sup>

### B. Annealing of graphene-ZnO NR/NW Hybrids

The post-growth annealing experiments of the graphene-ZnO NR/NW samples were performed under high vacuum ( $1.0 \times 10^{-5}$  mbar) and an Ar gas atmosphere (50 sccm flow rate) at two different temperatures (500 and 700 °C). The time duration of annealing was 2 and 1 h for vacuum and the Ar

gas atmosphere, respectively. Note that the PL results of graphene-ZnO NR/NW samples are discussed for the as-grown and 700 °C annealed samples in the present work. Visible PL from 500 °C annealed samples was reported in our previous work.<sup>15</sup>

### III. CHARACTERIZATION

The morphology and crystal structure of the as-grown and annealed samples were characterized by FESEM (Sigma, Zeiss) and XRD (Rigaku RINT 2500 TRAX-III, Cu K $\alpha$  radiation), respectively. The steady state PL spectra in the UV to visible region of all the samples were recorded with a 325 nm He-Cd laser excitation source using a commercial PL spectrometer (Fluorolog-3, Horiba) equipped with a photomultiplier tube detector. To compare the PL results, all the as-grown and annealed samples were measured under identical conditions. The visible-NIP PL spectrum was recorded using a 405 nm diode laser (Cube, Coherent) excitation source with the help of a spectrometer (focal length 30 cm; blaze wavelength 500 nm; groove density 150 g mm<sup>-1</sup>) equipped with a cooled CCD detector (Princeton Instruments, PIXIS 100B). Each spectrum was corrected with the detector response. XPS measurements were carried out with a fully automated XPS microprobe (PHI-Xtool, Ulvac-Phi, Japan) using an Al K $\alpha$  X-ray beam (1486.7 eV). The carbon 1s spectrum was used for the calibration of the XPS spectra recorded for various samples. Diffused reflectance spectroscopy (DRS) measurements were carried out using a commercial spectrometer (SolidSpec, Shimadzu) equipped with an integrating sphere. Photoconductivity (PC) measurements were performed using a microprobe station (ECOPIA EPS-500) connected to a source meter (Keithley 2400) for current-voltage (I-V) characteristics, and a 300 W Xenon lamp was used as a light source to excite the sample. Note that the excitation wavelength of incident light was chosen using a manual monochromator (Oriol Instruments, USA). The I-V setup is interfaced with a computer to collect the data using Lab Tracer 2.0 software.

### IV. RESULTS AND DISCUSSION

#### A. Structural studies

The morphological features of as-grown and annealed samples of graphene-ZnO NRs/NWs are investigated by high resolution FESEM imaging. Figure S1(a) shows the FESEM image of the as-grown ZnO NRs on the graphene substrate (GRZNR), and the size distribution of the ZnO NRs is shown in Fig. S1(b). It shows that the ZnO NRs with hexagonal facets have an average diameter of  $\sim 140$  nm and length of  $\sim 2.0$   $\mu\text{m}$ . Thus, the ZnO NRs have an aspect ratio of  $\sim 14$ . Figure S1(c) shows the TEM image of a single as-grown ZnO NW in GRZNW, which shows a diameter of  $\sim 35$  nm. The TEM image shows the simultaneous presence of graphene and ZnO NWs. Figure S1(d) shows the HRTEM lattice image of a single ZnO NW, showing the single crystalline nature of the as-grown NW. More details of the morphological features of the as-grown ZnO nanostructures are reported elsewhere.<sup>15</sup> Note that the underlying graphene

layer provides a kind of artificial epitaxy for the growth of hexagonal faceted ZnO NRs, as reported earlier.<sup>15</sup> Figure 1 shows the tilted view FESEM images of the vertically aligned hexagonal faceted ZnO NRs and NWs after annealing. Figures 1(a)–1(c) present the FESEM images of the 700 °C Ar gas annealed GRZNR, GRZNW (on graphene substrate), and ZNW (SiO<sub>2</sub> substrate) samples, respectively. The inset in each figure presents the high resolution FESEM image of the ZnO NRs/NWs to highlight the morphological features of the NRs/NWs after annealing. After annealing, there is no significant change in the morphology of the GRZNW and ZNW samples, while a distinct change in the surface morphology is observed for GRZNR, as shown in Fig. 1(a). In general, the

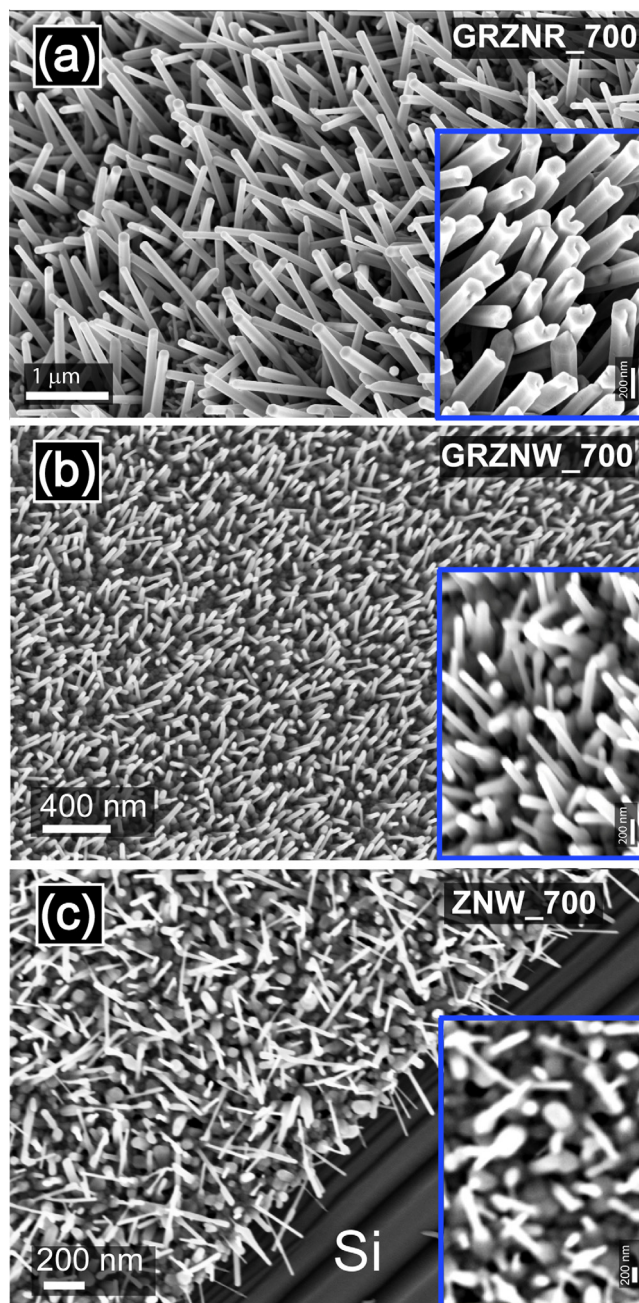


FIG. 1. FESEM images showing the morphological features of Ar-annealed (700 °C) samples: (a) graphene-ZnO NRs, (b) graphene-ZnO NWs, and (c) ZnO NWs-SiO<sub>2</sub>. The inset in each case depicts the higher magnification image of the same.

surface curvature of the hexagonal faceted ZnO NRs looks smoother after the annealing, while the higher resolution imaging shows that the tips of the ZnO NRs are split up in some regions possibly due to the splitting of catalyst Au NPs after the annealing, which leads to disorder on the NR surface [see the inset of Fig. 1(a)]. This may increase the effective surface to volume ratio of the ZnO NRs in GRZNR.

Further, XRD studies have been carried out to assess the improvement in the crystalline quality of the samples after annealing. Figure 2 presents the XRD pattern of the annealed graphene-ZnO NR/NW hybrids. In as-grown and annealed samples, a strong peak at  $2\theta = 34.5^\circ$  corresponding to the (0002) plane of ZnO signifies the crystalline wurtzite structure of aligned ZnO NRs/NWs.<sup>15</sup> Note that there are some secondary phases in the XRD pattern due to the unreacted Zn present after the VLS growth of ZnO NWs from the Zn source metal. This is due to adoption of a relatively low temperature (540 °C) growth process for the ZnO NRs/NWs.

## B. XPS studies

XPS measurements were carried out to identify the elemental composition and local environment of defects in the as-grown and post-growth annealed graphene-ZnO NR/NW hybrids. The characteristic XPS features of GRZNR, GRZNW, and ZNW samples are shown in Fig. 3. It presents the core level spectra of graphene (C-1s) and ZnO (Zn-2p, O-1s) in GRZNR (Fig. 3(a), GRNW [Fig. 3(b)] and ZNW [Fig. 3(c)]. The corresponding fitting parameters are presented in Table I. Interestingly, all the samples show a very

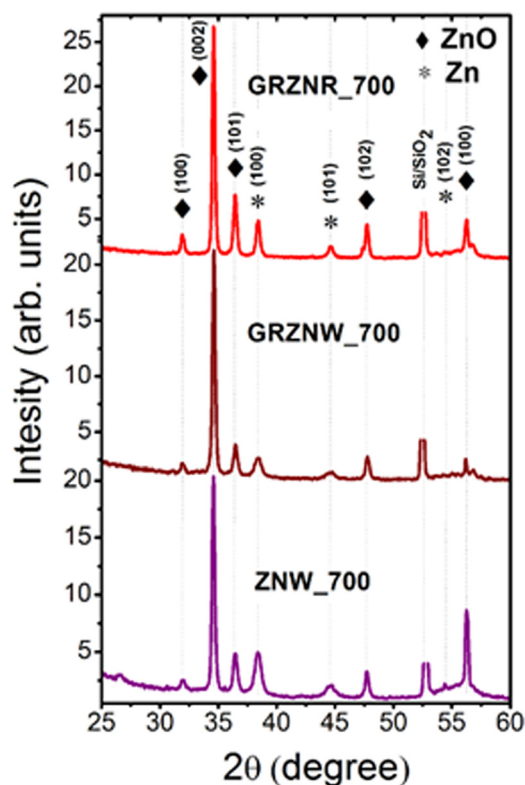


FIG. 2. XRD patterns of the ZnO NRs/NWs on graphene and ZnO NWs on the Si/SiO<sub>2</sub> substrate after post growth annealing at 700 °C in the Ar atmosphere.

high oxygen content as compared to the Zn content. Thus, excess oxygen may be present in the form of O<sub>i</sub> and O<sub>Zn</sub> in the as-grown and annealed ZnO NRs/NWs. Note that the PL data (discussed later) showing strong visible PL in all the samples may be due to the excess oxygen related defects in the ZnO lattice, as revealed by the XPS analysis. XPS analysis (see Table I) shows that GRZNR contains the highest percentage of excess oxygen among all three samples. Interestingly, PL data (discussed later) show very high intensity of visible as well as NIR PL in the GRZNR sample as compared to the GRZNW and ZNW samples. The peaks at lower binding energy (Peak 1 at 530.2 eV) in the O-1s core level XPS spectrum can be attributed to O<sup>2-</sup> of the wurtzite structure of the hexagonal Zn<sup>2+</sup> ions, and the O<sup>2-</sup> ions are surrounded by zinc atoms with the full supplement of nearest-neighbor O<sup>2-</sup> ions. The higher energy peak at 531.33 eV (Peak 2) is associated with the O<sup>2-</sup> ions in the oxygen-deficient regions within the ZnO matrix.<sup>25</sup> Thus, XPS spectrum reveals that as-grown ZnO NRs/NWs have oxygen rich as well as oxygen deficient regions in the same sample.<sup>15</sup> Due to the low energy of formation, oxygen vacancies are easily formed in ZnO crystals.<sup>26,27</sup> The deconvolution of the Zn-2p<sub>3/2</sub> core level XPS spectrum shows two peaks at 1021.58 and 1021.97 eV for GRZNR, as shown in Fig. 3(a). A similar deconvolution is shown in Figs. 3(b) and 3(c) for GRZNW and ZNW, respectively. The lower energy and higher energy components in each sample represent Zn in the oxide form and Zn in the metal form, respectively.<sup>25</sup> The centre of the XPS peaks and their respective identity are presented in Table I. The ratio of relative area of peak 2 to peak 1 in GRZNR is slightly higher (0.54) than that in GRZNW (0.44), i.e., Zn in the form of metal nanoparticles and/or Zn interstitials (Zn<sub>i</sub>) are present in higher concentration in GRZNR. This is fully consistent with the XRD patterns showing diffraction peaks at 38.37° (100), 44.58° (101), and 54.3° (102) (see Fig. 2) due to the unreacted Zn metal in both as-grown and annealed samples.<sup>15</sup> Thus, despite good crystallinity and hexagonal facets of the ZnO NRs, as-grown ZnO NRs and NWs show a high concentration of oxygen and zinc related defects. In particular, intrinsic defects O<sub>i</sub>, O<sub>Zn</sub>, V<sub>O</sub>, and V<sub>Zn</sub> may be high in these samples. Due to the relatively low growth temperature adopted here, the surface defect density might be high in these samples.

## C. UV and visible PL studies

The absorption spectra of ZnO NRs/NWs on graphene substrates were extracted from the Kubelka-Munk function derived from the DRS measurement (see Fig. S2, [supplementary material](#)). All the samples show strong absorption below 365 nm. UV and visible PL spectra of the as-grown and annealed (700 °C, Ar atmosphere) graphene-ZnO NR/NWs are first recorded using 325 nm, the above band-gap excitation. The room temperature PL spectra of GRZNR, GRZNW, and ZNW, after annealing, are shown in Figs. 4(a)–4(c), respectively. Note that the PL results of the as-grown ZnO NRs/NWs on graphene substrates were reported earlier.<sup>15</sup> All the samples show a distinct UV and relatively strong broad visible PL band before as well as after post-growth annealing. The symbols correspond to the experimental data, and the

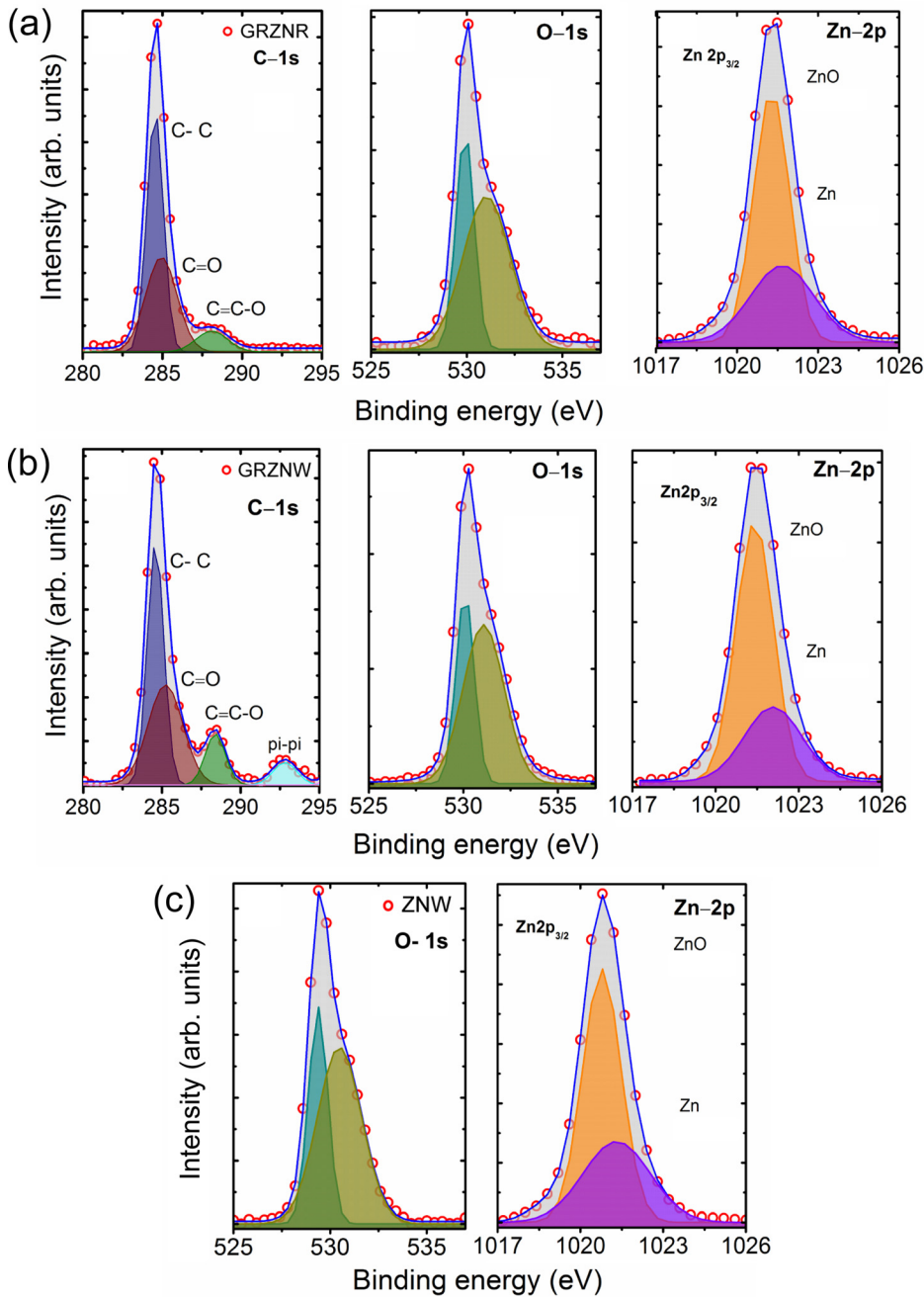


FIG. 3. Core level XPS spectra of (a) GRZNR, (b) GRZNW, and (c) ZNW samples, showing the deconvoluted C1s peaks arising from graphene and O-1s and Zn-2p peaks of ZnO NRs. Integrated intensity (areas) of individual components of fitted peaks in each spectrum signifies the contribution of each element and their bonding in the respective samples.

solid line refers to the fitted spectrum in each case (Fig. 4). We observed the UV emission peak at 375–377 nm and the visible PL band centered at  $\sim 500$  nm, which are attributed to the near band edge emission (NBE) and intrinsic defect states of the ZnO NRs/NWs, respectively. The sharp NBE peak at  $\sim 375$  nm signifies the good crystallinity of the as-grown ZnO NRs/NWs. The centre of the visible PL band differs from sample to sample, while the center of the UV peak is almost identical in all the samples and it remains unchanged even after annealing. Note that after annealing, besides the NBE peak, the UV band shows a small peak (P1\*) at 384–391 nm, probably related to the surface states.<sup>28</sup> It appears that the surface states become more active and nonradiative channels are reduced after annealing. The broad visible PL is a signature of various intrinsic defects in ZnO nanostructures, such as  $V_{O_i}$ ,<sup>29</sup>  $O_i$ ,<sup>30</sup> or  $Zn_i$ <sup>26</sup> interstitials and antisite oxygen ( $O_{Zn}$ )<sup>31–33</sup>

defects. Various PL peaks and probable identities of each peak are summarized in Table II, based on our analysis and literature reports.

It may be noted that the intrinsic defects are formed during the growth of the ZnO NWs, particularly due to the adoption of relatively lower growth temperature ( $540^\circ\text{C}$ ) in the present work. In GRZNR, we observed about two orders of magnitude enhancement in the intensity of visible PL after  $700^\circ\text{C}$  annealing in the Ar environment, while in the case of GRZNW and ZNW, it was enhanced by a factor of 5 and 32, respectively. Interestingly, UV PL intensity was enhanced in all samples, and the ratio of intensities of UV to various visible PL emissions was significantly increased after annealing. In particular, the relative intensity of peak P1 with respect to that of peaks P4 and P5 is increased by about one order of magnitude in GRZNR after annealing, as shown in Table II.

TABLE I. Details of the fitting parameters for O 1s and Zn 2p core level XPS spectra of graphene-ZnO hybrid nanostructures. The atomic percentage of O and Zn in various samples as determined from XPS data is shown for comparison.

Sample	O-1s		Zn-2p		Atomic percentage	
	Peak1 (eV)	Peak2 (eV)	Peak1 (eV)	Peak2 (eV)	O1s (%)	Zn2p (%)
GRZNR	530.2	531.33	1021.58	1021.97	70.3	29.7
GRZNW	529.53	530.42	1021.7	1022.37	67.1	32.9
ZNW	529.68	530.48	1021.08	1021.6	63	37
Identity	$O^{2-}$	$V_o$	Zn-O	Zn metal		

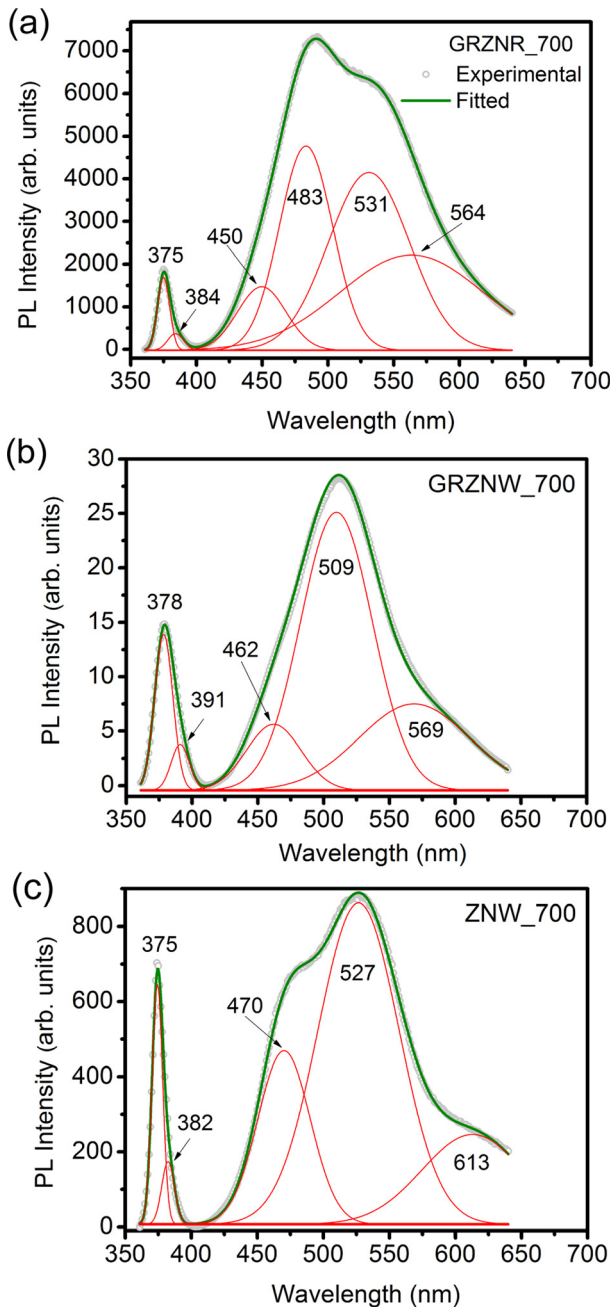


FIG. 4. Comparison of the PL spectra excited with the 325 nm laser for graphene and ZnO hybrid structures after Ar annealing at 700 °C: (a) GRZNR, (b) GRZNW, and (c) ZNW. UV and visible PL peaks are fitted with Gaussian line shapes, the symbols represent the experimental data, and the solid line corresponds to the fitted data.

It implies that after annealing, there is a significant improvement in the crystalline quality and reduction of nonradiative defects in the ZnO NRs/NWs. However, the density of radiative defects is increased considerably after annealing as evidenced from the overall increase in the visible PL intensity. Based on the literature reports, we tentatively assign the PL band appearing in the range of 447–468 nm to doubly ionized zinc vacancies ( $V_{Zn}^{2-}$ ),<sup>31</sup> and this is fully consistent with the XPS data discussed above. Note that this peak appears in all the samples before and after annealing, except for the as-grown GRZNR, and it may be due to the formation of ionized Zn vacancies or unreacted Zn leftover in the recrystallization process during the growth. The PL peaks in the range of 483–508 nm, commonly referred to as green emission, is observed in various ZnO nanostructures. Most of the theoretical and experimental reports propose that the green emission originates from either  $V_o$  or  $V_{Zn}$ .<sup>18,31,32,34,35</sup> Based on our XPS analysis, it is most likely to be assigned to  $V_{Zn}$  defects in ZnO. Interestingly, we also observed yellow (528–561 nm) and orange (613) PL emissions with 325 nm excitation, which are likely to originate from the deep levels of neutral  $O_{Zn}/O_i$  and ionized  $O_i$  induced transitions, respectively.<sup>30,32,36</sup> Note that these defects are very stable in the ZnO NRs/NWs since the visible PL intensity is high even after 700 °C annealing. Due to broad band visible PL emission at room temperature from these ZnO NRs/NWs, these hybrid structures are suitable for white light display and other optoelectronic device applications.

#### D. Near infrared PL studies

In order to investigate the nature of defects and their exact identity in graphene-ZnO NR/NW hybrids, we have conducted the PL measurements with below band-gap excitation on both as-grown and annealed samples. We used a 405 nm sub-band gap laser excitation source to monitor the visible-NIR PL spectra at room temperature. Figure 5 shows the room temperature PL spectra of the as-grown and 700 °C Ar annealed GRZNR [Figs. 5(a) and 5(b)], GRZNW [Figs. 5(c) and 5(d)], and ZNW [Figs. 5(e) and 5(f)] samples. Note that sub-band gap excitation gives rise to a large number of visible PL bands and additional NIR PL bands from the hybrid nanostructures. Due to the asymmetry in the line shape and its evolution, each PL spectrum is fitted with multiple Gaussian peaks. The symbols correspond to experimental data, and the solid green line refers to the fitted peak. The PL spectrum of each sample with above band-gap and below band-gap excitation shows common peaks in the range of 400 to 650 nm. Since we used a cooled CCD Si detector for monitoring the PL spectrum with sub-band gap excitation, additional distinct peaks are observed in the range of 650–900 nm. With 405 nm excitation, the blue, green, and orange-red emissions centered at ~450–486, ~500–563, and ~640–700 nm, respectively, are strong in all the as-grown as well as annealed samples. Figures S3(a) and S3(b) (supplementary material) show the Raman and PL spectra of the graphene/SiO<sub>2</sub> substrate, which are recorded to ascertain the quality of the graphene layer on which ZnO NRs and NWs were grown and to isolate the PL contribution arising solely

TABLE II. Details of the PL peaks (excitation wavelength 325 nm) fitted with Gaussian line shapes for the UV and visible emission bands of different samples before and after 700 °C Ar annealing. The center of each peak (P1–P5) is denoted in nm units. A14 and A15 denote the ratio of integrated intensity of UV peak to peaks P4 and P5, respectively.

Sample	As-grown							Annealed							
	P1	P2	P3	P4	P5	A14	A15	P1	P1*	P2	P3	P4	P5	A14	A15
GRZNR	376	...	486	542	577	0.06	0.1	375	384	450	483	532	557	0.6	0.7
GRZNW	377	468	500	543	...	0.13	...	378	391	462	509	...	569	0.1	0.3
ZNW	375	467	506	535	598	0.15	3.3	375	382	470	...	527	613	0.1	0.4
Identity	NBE	$V_{Zn}^{2-}$	$V_o/V_{Zn}$	$O_i/O_{zn}$	$O_i^-$			NBE	Band tail States	$V_{Zn}^{2-}$	$V_o/V_{Zn}$	$O_i/O_{zn}$	$O_i^-$		

from the ZnO NRs/NWs, respectively. The graphene/SiO<sub>2</sub> substrate shows two weak PL bands centered at 545 and 598 nm. Thus, in order to avoid the effect of the substrate and any other contaminants, such as the effect of residual PMMA, if any, the substrate PL spectrum was subtracted as the background from the PL spectrum of each hybrid ZnO NR/NW samples. However, sample PL intensity is much higher than the intensity of the PL from the substrate. Note that after annealing, the intensity of the orange-red emission is nearly doubled in GRZNR and ZNW, while it is not changed significantly in GRZNW. A summary of the PL

peak positions and their possible identities, based on the discussion in Sec. IV C, is presented in Table III.

Interestingly, a new PL emission band in the NIR range of 785–886 nm is observed in all the samples with the 405 nm sub-band excitation. The center of the peak for the NIR band slightly changes from sample to sample, due to contributions mainly from two components. Due to the asymmetric line shape of the PL band, two Gaussian peaks are fitted in each case (Fig. 5). Note that both NIR peaks appear above 800 nm, which is not reported earlier. A previous report on NIR PL in ZnO thin films discussed about a

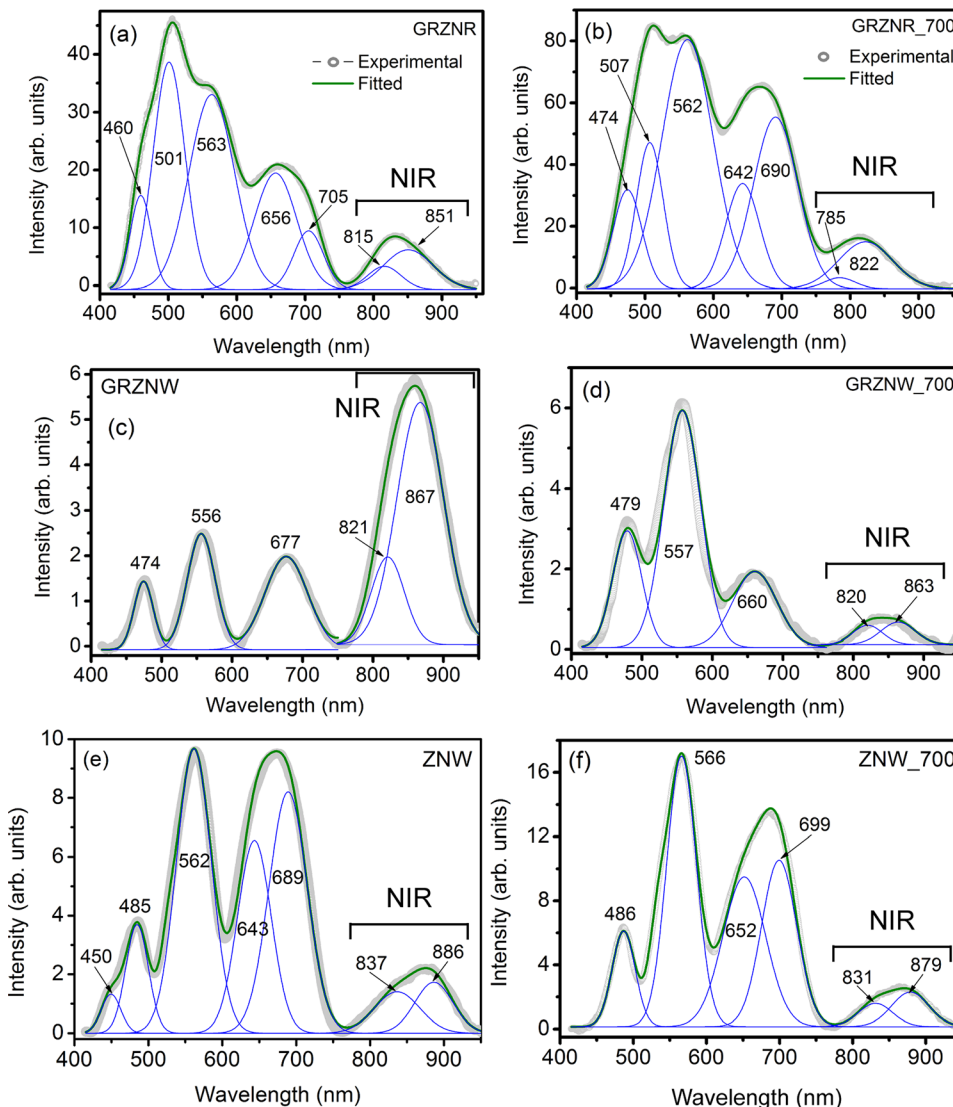


FIG. 5. Comparison of the visible and NIR PL spectra recorded with 405 nm excitation (sub-band gap) from different samples before and after annealing at 700 °C in Ar gas: (a) and (b) GRZNR, (c) and (d) GRZNW, and (e) and (f) ZNWs. Various peaks are fitted by Gaussian line shapes; the symbols represent the experimental data, and the solid line shows the fitted data. The new NIR PL band is marked in each case.

TABLE III. Details of the visible and NIR PL peaks fitted with Gaussian line shapes obtained with the sub-band gap excitation (405 nm) for each sample before and after 700 °C Ar annealing. The center of each peak is denoted in nm units. The identity (tentative) of each peak is written as per the standard notations used in the text. Note: \* indicates the new NIR peak.

Sample	As-grown							Annealed						
	<i>P1</i>	<i>P2</i>	<i>P3</i>	<i>P4</i>	<i>P5</i>	<i>P6*</i>	<i>P7*</i>	<i>P1</i>	<i>P2</i>	<i>P3</i>	<i>P4</i>	<i>P5</i>	<i>P6*</i>	<i>P7*</i>
GRZNR	460	501	563	...	705	815	851	474	507	562	642	690	785/822	...
GRZNW	474	...	556	...	677	821	867	479	...	557	660	...	820	863
ZNW	450	485	562	643	689	837	886	...	486	566	652	699	831	879
Identity	$V_{Zn}^{2-}$	$V_o/V_{Zn}$	$O_i$	$Zn_o$	$Zn_o/V_o$	$O_i^-$	$O_i$	$V_{Zn}^{2-}$	$V_o/V_o/V_{Zn}$	$O_i/O_{Zn}$	$Zn_o$	$Zn_o/V_o$	$O_i^-$	$O_i$

peak at  $\sim 756$  nm.<sup>18</sup> Our results are distinctly different, due to the use of sub-band gap excitation and the adoption of a different methodology of growth of ZnO NRs/NWs. Interestingly, after Ar annealing, the intensity of the NIR PL band is nearly doubled in GRZNR, while it is reduced in the GRZNW. Note that the relative intensities of two peaks are changed after annealing, with a minor change in the peak positions. The difference in peak positions for different samples may be due to their distinct structural morphology and the local environment of the defects in the ZnO lattice.

Note that the NIR band in general has received far less attention in the literature, although some groups<sup>18,22</sup> have reported NIR PL at  $\sim 750$  nm (1.65 eV) in ZnO thin films, while we observed the NIR PL bands at above 800 nm. In some cases, the NIR PL band is ascribed to the second order diffraction of UV PL, as it can only be observed in the ZnO films with a strong UV luminescence. However, it has also been postulated that the NIR PL originates from the oxygen related defects similar to those responsible for the red luminescence in ZnO.<sup>18,22</sup> The possibility of second order diffraction of UV PL manifesting as a NIR PL band at  $\sim 850$  nm is completely ruled out here since we used a 405 nm excitation source in the present study. Note that the graphene layer has no contribution to the observed NIR PL since the graphene is a zero band gap material. There is a possibility that graphene oxide (GO) is formed during the ZnO NW growth under oxygen flow and GO may contribute to the weak visible PL. However, to our knowledge, there is no report on the NIR PL from the GO layer, if at all present here. In some of our experiments, we find the formation of GO during the vapor transport experiment. Note that GO shows a broad visible PL under UV excitation, which can be attributed to various oxygenated functional groups present on the basal plane of graphene. Thus, observed NIR PL is believed to arise from the intrinsic defects in the ZnO NRs.

Based on the XPS analysis, the possibility of NIR PL originating from the oxygen interstitial defects is quite likely in the present case. Interestingly, as-grown GRZNW shows a strong NIR PL band at 867 nm, and its intensity is strongly reduced (by about 5 times) after annealing in the Ar ambient, which may be due to the reduction in neutral  $O_i$  defects in the annealed samples.<sup>26,35</sup> The two PL components with centers at 820–830 nm and 863–879 nm are tentatively attributed to  $O_i^-$  and neutral  $O_i$ , respectively.<sup>35</sup> Despite the post-growth annealing, the defect related PL intensity is strong in the GRZNR sample because of a high oxygen content and a

large surface area of ZnO NRs with the split tips that may contain a high density of traps on the surface.

To clarify further the origin of NIR PL and its relation to  $O_i$  induced defects in ZnO NRs/NWs, vacuum annealing of GRZNR samples was conducted and PL emission was studied with both above band-gap (355 nm) excitation and below band-gap excitation (405 and 488 nm) to monitor the evolution of UV, visible, and NIR PL emissions. Figure 6(a) shows a comparison of the PL spectra recorded with 355 nm excitation for the GRZNR sample after vacuum ( $1.0 \times 10^{-5}$  mbar) annealing at 500 and 700 °C. The data clearly show that there is a systematic reduction in the intensity of the green emission and enhancement in the intensity of the UV emission band with the increasing temperature of vacuum annealing. Interestingly, no NIR PL band could be detected in the vacuum annealed sample, indicating the deactivation/partial removal of the associated defects. Figure 6(b) shows the PL spectrum of the 700 °C annealed sample recorded with 405 nm excitation, and the broad asymmetric PL peak could be fitted with three Gaussian peaks centered at 481, 540, and 602 nm. The visible PL bands are found to be consistent with those shown in Fig. 5. In fact, the major reduction in the  $O_i$  induced peak ( $\sim 540$  nm) of GRZNR after vacuum annealing along with the disappearance of the NIR PL peaks is consistent with our argument that the NIR PL arises from the  $O_i$  defects in ZnO. The absence of NIR PL was further confirmed from the vacuum annealed GRZNR sample excited with the 488 nm laser, as shown in Fig. 6(c). It shows only visible PL centered at 638 nm, and no NIR PL was detectable. Thus, the vacuum annealing possibly eliminates the  $O_i$  defects in the ZnO NRs/NWs, and our PL assignments are consistent with the annealing results.

### E. Time resolved PL studies

The time resolved PL measurement of the Ar gas annealed GRZNR, GRZNW, and ZNW samples was carried out to understand PL decay dynamics of the  $V_o/O_i$  induced states with the green emission (500 nm) under the excitation of a 375 nm pulsed laser source. Figure 7(a) shows the PL decay behavior of different samples monitored at 500 nm. Sample GRZNR shows relatively slow decay of PL with three components having time constants 1.45, 10.4, and 604.5 ns, where the amplitude of the fastest component (1.42 ns) dominates the decay. However, GRZNW and ZNW samples show a relatively faster decay with a bi-exponential decay having time constants 1.42 and  $\sim 8.0$  ns and 1.40 and

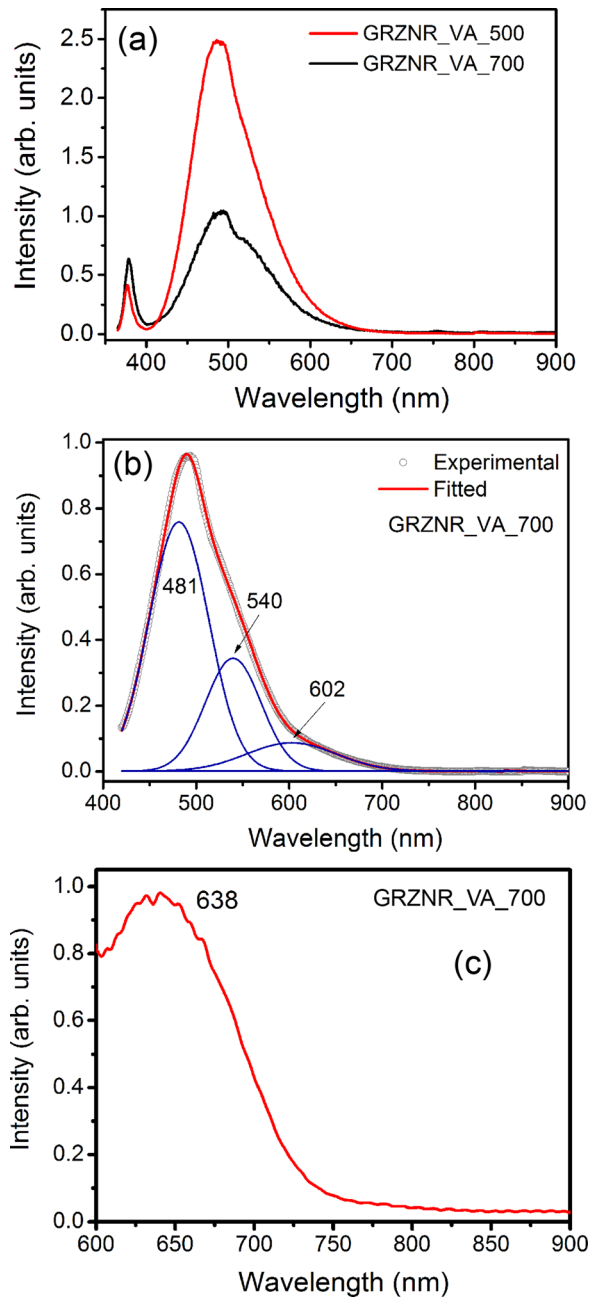


FIG. 6. PL spectra of the vacuum annealed GRZNR sample excited with different laser wavelengths: (a) 325 nm excitation for 500 and 700 °C vacuum annealed samples and (b) 405 nm excitation for 700 °C vacuum annealed GRZNR. Symbols represent the experimental data, and the solid line shows the fitted peak. (c) 488 nm excitation for 700 °C vacuum annealed GRZNR. The peak position is denoted in nm units. Note that no NIR PL was detectable after vacuum annealing.

4.7 ns, respectively. Interestingly, the first two components of the PL decay are common to all samples, and these correspond to the green emission bands centered at  $\sim 500$  nm and  $\sim 530$  nm, as shown in Table II and Fig. 4. These peaks/decay components correspond to  $V_o/V_{Zn}$  and  $O_i/O_{Zn}$ , respectively. A similar timescale of decay has been reported for green emission in ZnO NW/NRs grown by the standard VLS method.<sup>28</sup> Note that the GRZNR sample shows an additional slow decay component with a large time constant of 604.5 ns, and this may be due to the strong PL peak at  $\sim 560$  nm (see Fig. 5 and Table III) that was tentatively assigned to the  $O_i$  defects in

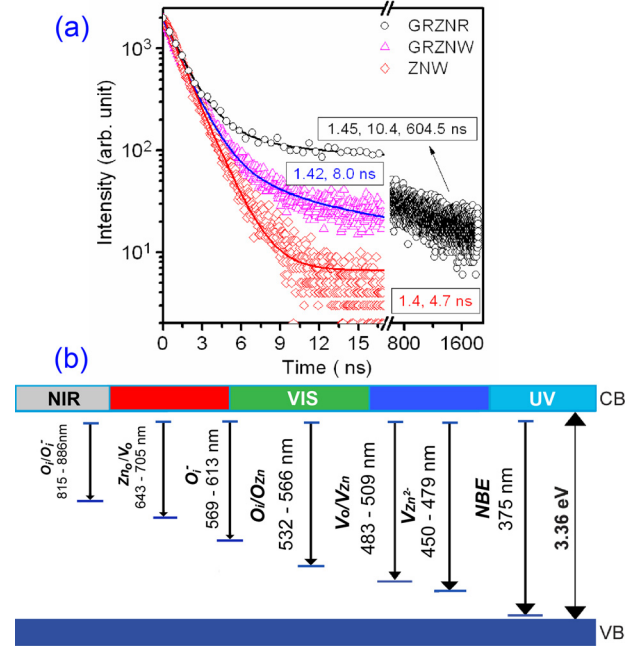


FIG. 7. (a) Time resolved PL decay measured at 500 nm (green emission) in Ar annealed GRZNR, GRZNRW, and ZNW samples excited with 375 nm excitation. The symbols represent the experimental data, and the solid line represents the multi-exponential fit to the data. (b) A schematic of the energy band diagram showing various defect states in the band gap of ZnO NRs/NWs grown on graphene and the corresponding PL emission wavelengths reported in this work.

ZnO. Thus, the recombination of carriers at the neutral  $O_i$  appears to be very slow. This may be due to the recombination of a shallowly trapped electron with a deeply trapped hole at  $V_{Zn}$  and  $O_i$ , as discussed in the literature.<sup>18,21,31</sup> Recent transient absorption spectroscopy on ZnO has demonstrated that the green emission originates from the recombination between the electrons at the conduction band and/or shallow donor (sub-band-gap) levels and the holes trapped at the green emission centers.<sup>21,37</sup> If the sub-band-gap states behave as a shallow trap, the decay rate of the emission process will become slower since the electron in the sub-band-gap states cannot directly be transferred to the emission state but will experience a thermally activated trapping/detrapping process before finally relaxing to the emitting state. Under the above assumption, PL decay is expected to be slow especially under below-band-gap excitation because of a prolonged transport period associated with the relevant trapping/detrapping process. Our observation of a slow decay component (time constant  $\sim 604.5$  ns) is consistent with this interpretation. The results of the steady state PL and time resolved PL are found to be consistent. The nature and origin of various PL emission bands in ZnO NRs/NWs discussed above can be summarized by the schematic energy band diagram shown in Fig. 7(b), following the report by Wang *et al.*<sup>18</sup> The presence of a large number of highly stable defect centres emitting in the visible and NIR region makes the graphene-ZnO hybrid suitable for bright display applications. We have demonstrated the tunability of the PL emission bands through controlling the growth parameters and the post-growth processing conditions.

**F. Photoconductivity studies**

To evaluate the role of surface defects in the ZnO NRs/NWs in the photophysical processes in graphene-ZnO NR/NW hybrids, photoconductivity (PC) measurements were carried out on the annealed samples of ZnO NR/NW samples. Figure 8(a) shows a schematic of the photoconductivity/photoresponse measurement setup and the device structure of graphene and the ZnO NR/NW hybrid. Figures 8(b) and 8(c) present the dark current and photocurrent characteristics of the annealed GRZNR and GRZNW samples as a function of sweep voltage. Here, in both ZnO NWs and NRs, the background current (dark current) is considerably low ( $\sim 1.5 \pm 0.5 \mu\text{A}$ ) even at high bias voltage [see Figs. 8(b) and 8(c)]. This might be due to the fact that a considerable amount of surface defects (mostly  $V_O$  and  $O_i$ ) is present on the ZnO NRs/NWs, which act as trap centers for the charge carriers. Note that the PC is strongly enhanced with UV illumination in both the GRZNR and GRZNW cases. The UV photo-response behavior as a function of time, illuminated with 370 nm excitation, is illustrated in Figs. 8(d) and 8(e). The time response curves

are fitted with bi-exponential growth and bi-exponential decay functions.<sup>11</sup> Note that the dotted lines represent the experimental data and the solid line represents the fitted data. The PC growth with time  $I_{ph}(t)$  can be represented by

$$I_{ph}(t) = I_1 + A_1(1 - e^{-\frac{t}{\tau_1}}) - A_2e^{-\frac{t}{\tau_2}}. \quad (1)$$

Here,  $I_1$ ,  $A_1$ , and  $A_2$  are the positive constants.  $\tau_1$  and  $\tau_2$  are the time constants, which are calculated from the fitting. In annealed GRZNR and GRZNW,  $\tau_1$  and  $\tau_2$  are found to be 14.8, 266.9 s and 9.9, 241.8 s, respectively. Similarly, the PC decay data can be fitted with a bi-exponential decay of the form

$$I_{ph}(t) = I_{ph}(\infty) + A_3e^{-\frac{t}{\tau_1}} + A_4e^{-\frac{t}{\tau_2}}. \quad (2)$$

Here,  $A_3$  and  $A_4$  are the constants.  $\tau_1$  and  $\tau_2$  are calculated to be 35.3, 852.1 s and 14.3, 360.8 s for GRZNR and GRZNW, respectively. Note that  $I_{ph}(\infty)$  represents the photocurrent after a longer duration of time, which is equal to the dark current. The data reveal that due to the multiple trapping by various oxygen-related defects, such as  $O_i$  and  $V_O$  in the ZnO

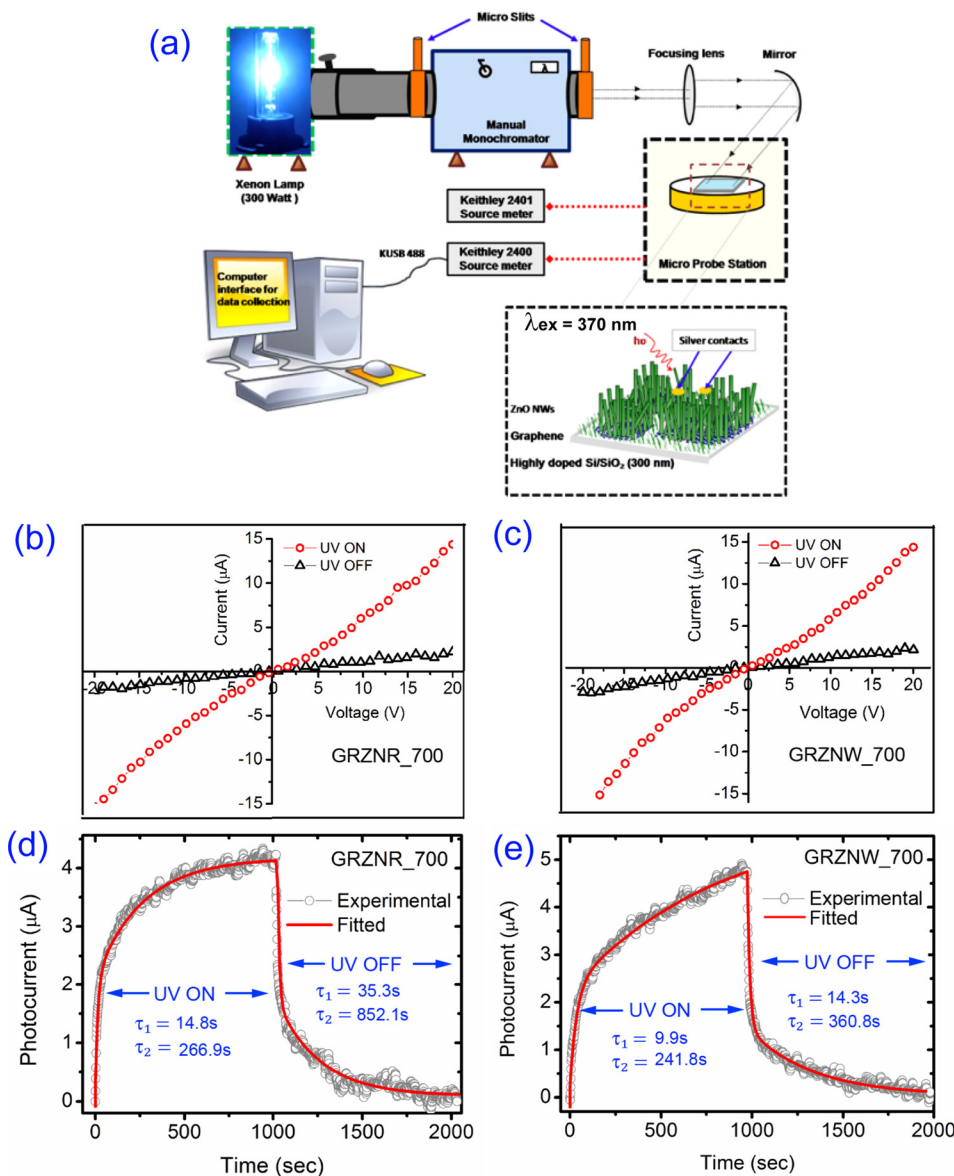


FIG. 8. (a) A schematic of the photoconductivity setup and graphene-ZnO NW device structure. (b) Dark current and photocurrent as a function of voltage for 700 °C Ar annealed GRZNR, (c) the same for 700 °C Ar annealed GRZNW, (d) and (e) the corresponding photocurrent time response. The excitation wavelength used for the photoconductivity measurement is 370 nm at a fixed bias voltage (8 V).

NRs/NWs, the PC decay and rise are slow. Note that the PC decay is relatively slow in GRZNR, which is consistent with the slow PL decay dynamics observed in the sample. We believe that the slow relaxation of the carriers is due to the presence of the  $O_i$  defects in large concentration. These results are consistent with the PL and XPS analyses discussed earlier.

## V. CONCLUSIONS

We have reported strong UV, visible, and NIR PL emission at room temperature from the as-grown and annealed samples of graphene-ZnO NR/NW hybrids. Strong NIR PL emissions in the range of 815–886 nm excited with sub-band gap excitation were reported from ZnO NRs/NWs grown on single layer graphene, for the first time. Based on the evolution of the visible and NIR PL peaks due to the annealing in vacuum and the Ar atmosphere at 700 °C, the NIR PL was assigned to the radiative recombination of shallowly trapped electrons with deeply trapped holes of neutral/ionized  $O_i$  induced radiative centers. The PL decay dynamics show an additional slow decay component, due to the shallow to deep transition at the  $O_i$  induced defects. The PL assignments are strongly supported by the XPS analysis of Zn-2p and O-1s spectra. Further, a slow photoresponse observed in the photoconductivity measurements from ZnO NRs/NWs is consistent with the dominance of oxygen related surface defects on the ZnO NRs/NWs. The tunable visible, NIR PL emission, and identification of the species responsible for the broad band visible and NIR PL emissions constitute an important milestone in exploring the new generation optoelectronic and bioimaging applications of graphene-ZnO NR/NW hybrids. Control of defects in CVD graphene and control of interface states would provide more insights into the future applications of these novel hybrid 2D-1D nanostructures of two powerful materials, namely, graphene and ZnO.

## SUPPLEMENTARY MATERIAL

See [supplementary material](#) for the FESEM and TEM image of the as-grown ZnO NRs and ZnO NWs (Fig. S1), results and discussion on the diffused reflectance spectrum of ZnO NRs/NWs, the PL spectrum of the graphene/SiO<sub>2</sub> substrate (Fig. S2), diffused reflectance spectrum of GRZNR, GRZNW, and ZNW samples (Fig. S2), and Raman and PL spectra of the graphene/SiO<sub>2</sub> substrate (Fig. S3).

## ACKNOWLEDGMENTS

We acknowledge the financial support from DEITY (No. 5(9)/2012-NANO, Vol-II), India, to carry out the part of this work. We acknowledge the financial support from CSIR (grant no. 02(1270)/13/EMR-II). We acknowledge the Central Instrument Facility (CIF) for providing the FESEM facility. We are grateful to Professor M. Fujii, Kobe University, Japan, for help in the XPS and PL measurements.

- <sup>1</sup>W. I. Park, C.-H. Lee, J. M. Lee, N.-J. Kim, and G.-C. Yi, *Nanoscale* **3**, 3522 (2011).
- <sup>2</sup>B. Kumar, K. Y. Lee, H. K. Park, S. J. Chae, Y. H. Lee, and S.-W. Kim, *ACS Nano* **5**, 4197 (2011).
- <sup>3</sup>H. Lee, K. Heo, J. Park, Y. Park, S. Noh, K. S. Kim, C. Lee, B. H. Hong, J. Jian, and S. Hong, *J. Mater. Chem.* **22**, 8372 (2012).
- <sup>4</sup>C.-J. Shih, Q. H. Wang, Y. Son, Z. Jin, D. Blankschtein, and M. S. Strano, *ACS Nano* **8**, 5790 (2014).
- <sup>5</sup>J. Lee, Y. B. Pyun, J. Yi, J. W. Choung, and W. Park, *J. Phys. Chem. C* **113**, 19134 (2009).
- <sup>6</sup>K. B. Ravi, T. Nikhil, R. Gone, S. Dhara, and P. K. Giri, *Nanotechnology* **26**, 145601 (2015).
- <sup>7</sup>P. Gowda, T. Sakorikar, S. K. Reddy, D. B. Ferry, and A. Misra, *ACS Appl. Mater. Interfaces* **6**, 7485 (2014).
- <sup>8</sup>S. G. Zhang, X. W. Zhang, F. T. Si, J. J. Dong, J. X. Wang *et al.*, *Appl. Phys. Lett.* **101**, 121104 (2012).
- <sup>9</sup>H. Park, S. Chang, J. Jean, J. J. Cheng, P. T. Araujo, M. Wang, M. G. Bawendi, M. S. Dresselhaus, V. Bulovic, J. Kong, and S. Gradecak, *Nano Lett.* **13**, 233 (2013).
- <sup>10</sup>S. Kim, D. B. Janes, S.-Y. Choi, and S. Ju, *Appl. Phys. Lett.* **101**, 063122 (2012).
- <sup>11</sup>S. Dhara and P. K. Giri, *Nanoscale Res. Lett.* **6**, 504 (2011).
- <sup>12</sup>S. Dhara and P. K. Giri, *J. Appl. Phys.* **110**, 124317 (2011).
- <sup>13</sup>M. Willander, O. Nur, N. Bano, and K. Sultana, *New J. Phys.* **11**, 125200 (2009).
- <sup>14</sup>S. Dhara and P. K. Giri, *Rev. Nanosci. Nanotechnol.* **2**, 147 (2013).
- <sup>15</sup>R. K. Biroju, P. K. Giri, S. Dhara, K. Imakita, and M. Fujii, *ACS Appl. Mater. Interfaces* **6**, 377 (2014).
- <sup>16</sup>S. Dhara and P. K. Giri, *Chem. Phys. Lett.* **541**, 39 (2012).
- <sup>17</sup>B. Buddha Deka, B. F. Darim, M. Anwasha, and M. Abha, *Nanotechnology* **26**, 235703 (2015).
- <sup>18</sup>M. Wang, Y. Zhou, Y. Zhang, E. J. Kim, and S. H. Hahn, *Appl. Phys. Lett.* **100**, 101906 (2012).
- <sup>19</sup>A. Bera and D. Basak, *Chem. Phys. Lett.* **476**, 262 (2009).
- <sup>20</sup>B. Panigrahy, M. Aslam, D. S. Misra, M. Ghosh, and D. Bahadur, *Adv. Funct. Mater.* **20**, 1161 (2010).
- <sup>21</sup>B. K. Meyer, H. Alves, D. M. Hofmann, W. Kriegseis, D. Forster, F. Bertram, J. Christen, A. Hoffmann, M. Straßburg, M. Dworzak, U. Haboeck, and A. V. Rodina, *Phys. Status Solidi B* **241**, 231 (2004).
- <sup>22</sup>T. Nguyen, N. T. Tuan, V. D. Nguyen, N. D. Cuong, N. D. T. Kien, P. T. Huy, V. H. Nguyen, and D. H. Nguyen, *J. Lumin.* **156**, 199 (2014).
- <sup>23</sup>Q. Zhu, C. Xie, H. Li, C. Yang, S. Zhang, and D. Zeng, *J. Mater. Chem. C* **2**, 4566 (2014).
- <sup>24</sup>R. K. Biroju and P. K. Giri, *J. Phys. Chem. C* **118**, 13833 (2014).
- <sup>25</sup>L. L. Yang, Q. X. Zhao, M. Willander, X. J. Liu, M. Fahlman, and J. H. Yang, *Appl. Surf. Sci.* **256**, 3592 (2010).
- <sup>26</sup>A. Janotti and C. G. Van de Walle, *Phys. Rev. B* **76**, 165202 (2007).
- <sup>27</sup>M. D. McCluskey and S. J. Jokela, *J. Appl. Phys.* **106**, 071101 (2009).
- <sup>28</sup>S. Dhara and P. K. Giri, *Funct. Mater. Lett.* **04**, 25 (2011).
- <sup>29</sup>K. Vanheusden, W. L. Warren, C. H. Seager, D. R. Tallant, J. A. Voigt, and B. E. Gnade, *J. Appl. Phys.* **79**, 7983 (1996).
- <sup>30</sup>B. Lin, Z. Fu, and Y. Jia, *Appl. Phys. Lett.* **79**, 943 (2001).
- <sup>31</sup>A. Janotti and C. G. Van de Walle, *J. Cryst. Growth* **287**, 58 (2006).
- <sup>32</sup>J. Liu, S. Lee, Y. H. Ahn, J. Y. Park, and K. H. Koh, *J. Phys. D: Appl. Phys.* **42**, 095401 (2009).
- <sup>33</sup>Ü. Özgür, Y. I. Alivov, C. Liu, A. Teke, M. A. Reshchikov, S. Doğan, V. Avrutin, S.-J. Cho, and H. Morkoç, *J. Appl. Phys.* **98**, 041301 (2005).
- <sup>34</sup>B. Guo, Z. R. Qiu, and K. S. Wong, *Appl. Phys. Lett.* **82**, 2290 (2003).
- <sup>35</sup>A. F. Kohan, G. Ceder, D. Morgan, and C. G. Van de Walle, *Phys. Rev. B* **61**, 15019 (2000).
- <sup>36</sup>D. Li, Y. H. Leung, A. B. Djuricic, Z. T. Liu, M. H. Xie, S. L. Shi, S. J. Xu, and W. K. Chan, *Appl. Phys. Lett.* **85**, 1601 (2004).
- <sup>37</sup>M. Li, G. Xing, G. Xing, B. Wu, T. Wu, X. Zhang, and T. C. Sum, *Phys. Rev. B* **87**, 115309 (2013).